International Journal of Solids and Structures 121 (2017) 228–239

Contents lists available at ScienceDirect

International Journal of Solids and Structures

journal homepage: www.elsevier.com/locate/ijsolstr

A deformation-theory based model of a damaged metal matrix composite

Ashish Mishra, Sivasambu Mahesh*

Department of Aerospace Engineering, Indian Institute of Technology Madras, Chennai, 600036 India

ARTICLE INFO

Article history:
Received 10 February 2016
Revised 24 March 2017
Available online 30 May 2017

Keywords:
Metal matrix composite
Unidirectional
Shear lag
Nonlinear
Failure

ABSTRACT

A shear-lag and deformation-theory based model for a metal matrix composite reinforced by continuous unidirectional fibres is proposed. The model accounts for fibre and matrix cracking, matrix plasticity, and fibre-matrix interfacial sliding through seven characteristic non-dimensional parameters, which combine geometric, phase and interface properties. It allows arbitrary tensile loading and unloading history along the fibre direction, and predicts the history-dependent elastoplastic displacement, strain, and stress fields in all the fibre and matrix elements. Broken elements may be present initially, or form during the imposed loading history. Non-linear one-dimensional governing differential and algebraic equations are formulated on the basis of the model. A computationally fast solution methodology based on pseudospectral collocation is implemented. The present model is employed to predict the elastic strain profiles in a Ti/SiC composite tape near pre-existing breaks. These predictions agree well with experimental measurements reported in the literature.

1. Introduction

In the low and intermediate pressure stages of aerospace gas turbines, considerable weight and cost associated with a compressor stage can be saved by replacing conventional superalloy discs with titanium (Ti) alloy matrix composite bladed compressor rings (Winstone et al., 2001; Martin and Carrére, 2012). Typically, continuous silicon carbide (SiC) fibres reinforce the Ti alloy matrix, as SiC fibres have excellent high temperature properties and long-term chemical compatibility with the Ti matrix material (Martin and Carrére, 2012). Failure of SiC/Ti alloy metal matrix composites occurs by the localised failure of nearby fibres, and is not preceded by much global damage (González and Llorca, 2001; Martin and Carrére, 2012), provided the fibre-matrix interface is sufficiently strong (Du and McMeeking, 1994). An accurate description of the stress distribution near damaged regions is essential to understand crack propagation in these materials. This description is best obtained by constructing a sufficiently detailed model of load transfer in partially damaged metal matrix composites, and by experimentally validating its predictions.

Microscopic damage in unidirectionally reinforced metal matrix composites takes the form of fibre breakages, matrix cracks, matrix yielding, and fibre-matrix interfacial debonding/sliding (Clyne and Withers, 1995). Models capable of representing some or all of these mechanisms have been developed in the literature, and allow classification into two broad groups. Models in the first group are based on the finite element method. These models resolve the detailed microstructure (Du and McMeeking, 1994; Landis and McMeeking, 1999; Xia et al., 2001; Xia and Curtin, 2001; González and Llorca, 2001), and incorporate complex constitutive laws for the various microstructural phases, and interfaces. They are able to predict spatially resolved mechanical fields in arbitrarily damaged metal matrix composites. However, the complexity of these models limits them to small volumes: Du and McMeeking (1994) and Landis and McMeeking (1999) assumed axisymmetric distribution of fibres around a broken fibre, and modelled three fibres only. González and Llorca (2001) modelled only three neighbours of a broken fibre in their finite element study of a single ply. The finite element models of Xia et al. (2001), treated nine and eleven fibre models arranged in a hexagonal array. A finite element model of a composite comprised of 400 fibres was utilised by Behzadi et al. (2009) to simulate composite failure. This model, however, treated the matrix as a multilinear elastic material, and did not account for plastic unloading.

The second group is comprised of shear-lag models. This class of models was pioneered by Cox (1952) for the stress state around a broken fibre surrounded by an axisymmetric matrix ring. The fibre, and matrix ring are bounded by a homogeneous effective composite medium. This simple model was considerably extended by

* Corresponding author.
E-mail addresses: ae13d212@smail.iitm.ac.in (A. Mishra), smahesh@iitm.ac.in (S. Mahesh).

http://dx.doi.org/10.1016/j.ijsolstr.2017.05.032
0020-7683/

Nomenclature

a	Fibre dimension, Fig. 1
A	Dimensionless parameter, Eq. (29)
A_f	Cross-sectional area of a fibre
b	Centre-to-centre distance between fibres, Fig. 1
B, C	Dimensionless parameters, Eq. (29)
d	Composite ply thickness, Fig. 1
E	Dimensionless parameter, Eq. (29)
E_f	Fiber elastic modulus, Eq. (4)
E_1	Matrix elastic modulus in tension, Eq. (5)
E_2	Matrix hardening modulus in tension, Eq. (5)
f_i	Fiber element i, Fig. 2
$\mathrm{f}_{\mathrm{sm}_k}$	Fibre element adjacent to the shear-matrix sm_k, Fig. 2
$\mathrm{f}^+_{\mathrm{tm}_j}$	Fibre element to the right of tensile-matrix tm_j, Fig. 2
$\mathrm{f}^-_{\mathrm{tm}_j}$	Fibre element to the left of tensile-matrix tm_j, Fig. 2
F	Dimensionless parameter, Eq. (29)
G_1	Matrix elastic modulus in shear, Eq. (13)
G_2	Matrix hardening modulus in shear, Eq. (13)
h	Surface-to-surface distance between adjacent fibres, Fig. 1
H	Dimensionless parameter, Eq. (29)
i, j, k	Elements indices
I, K	Dimensionless parameters, Eq. (29)
L	Composite length, Fig. 1
ℓ	Dimensionless fibrewise half-length of the composite, Eq. (37)
n	Exponent in the interfacial sliding law, Eq. (18)
n_C	Number of Chebyshev grid points Eq. (43)
n_f	Number of fibre elements
P	Total load imposed, Eq. (24)
$\hat{P}$	Dimensionless imposed load, Eq. (38)
s	Deformation step counter
$\mathrm{s}^+_{\mathrm{f}_i}$	Slider element to the right of fibre f_i, Fig. 2
$\mathrm{s}^-_{\mathrm{f}_i}$	Slider element to the left of fibre f_i, Fig. 2
s_k	Slider element k, Fig. 2
$\mathrm{s}_{\mathrm{sm}_k}$	Slider element adjacent to the shear-matrix sm_k, Fig. 2
$\mathrm{s}^+_{\mathrm{tm}_j}$	Slider element to the right of tensile-matrix tm_j, Fig. 2
$\mathrm{s}^-_{\mathrm{tm}_j}$	Slider element to the left of tensile-matrix tm_j, Fig. 2
$\mathrm{sm}^+_{\mathrm{f}_i}$	Shear-matrix element to the right of fibre f_i, Fig. 2
$\mathrm{sm}^-_{\mathrm{f}_i}$	Shear-matrix element to the left of fibre f_i, Fig. 2
sm_k	Shear-matrix element k, Fig. 2
$\mathrm{sm}^+_{\mathrm{tm}_j}$	Shear-matrix element to the right of tensile-matrix tm_j, Fig. 2
$\mathrm{sm}^-_{\mathrm{tm}_j}$	Shear-matrix element to the left of tensile-matrix tm_j, Fig. 2
$\mathrm{tm}^+_{\mathrm{f}_i}$	Tensile-matrix element to the right of fibre f_i, Fig. 2
$\mathrm{tm}^-_{\mathrm{f}_i}$	Tensile-matrix element to the left of fibre f_i, Fig. 2
tm_j	Tensile-matrix element j, Fig. 2
$\mathrm{tm}_{\mathrm{sm}_k}$	Tensile-matrix element adjacent to the shear-matrix sm_k, Fig. 2
w_{f_i}	Displacement of the ith fiber element, Eq. (1)
$\hat{w}_{\mathrm{f}_i}$	Dimensionless displacement of the ith fiber element, Eq. (28)
w_{tm_j}	Displacement of the jth tensile-matrix element, Eq. (2)
$\hat{w}_{\mathrm{tm}_j}$	Dimensionless displacement of the jth tensile-matrix element, Eq. (28)
w_{s_k}	Displacement of the kth slider element, Eq. (3)
$\hat{w}_{\mathrm{s}_k}$	Dimensionless displacement of the kth slider element, Eq. (28)
W	Dimensionless parameters, Eq. (29)
x	Co-ordinate normal to the fibre direction, Fig. 1
z	Co-ordinate parallel to the fibre direction, Fig. 1
γ_{round}, γ_{shift}	Numerical smoothing parameters, Eq. (16)
γ_{sm_k}	Shear strain in shear-matrix element k, Eq. (3)
$\gamma^{\mathrm{pl}}_{\mathrm{sm}_k}$	Plastic shear strain in the shear-matrix element k. Eq. (15)
$\hat{\gamma}^{\mathrm{pl}}_{\mathrm{sm}_k}$	Dimensionless plastic shear strain in the shear-matrix element k, Eq. (31)
$\gamma^{\mathrm{peak}}_{\mathrm{sm}_k}$	Peak shear strain in shear-matrix element k, Eq. (16)
$\varepsilon_{\mathrm{round}}$	Numerical smoothing parameter, Eq. (11)
$\varepsilon_{\mathrm{engg}}$	Imposed engineering strain, Eq. (23)
ϵ_{f_i}	Axial strain in fibre element i, Eq. (1)
$\varepsilon_{\mathrm{tm}_j}$	Axial strain in tensile-matrix element j, Eq. (2)
$\varepsilon^{\mathrm{el}}_{\mathrm{tm}_j}$	Elastic strain in the tensile-matrix element j, Fig. 3
$\varepsilon^{\mathrm{pl}}_{\mathrm{tm}_j}$	Plastic strain in the tensile-matrix element j, Fig. 3
$\hat{\varepsilon}^{\mathrm{pl}}_{\mathrm{tm}_j}$	Dimensionless plastic axial strain in the tensile-matrix element j, Eq. (33)
$\varepsilon^{\mathrm{peak}}_{\mathrm{tm}_j}$	Peak axial strain in the tensile-matrix element j, Fig. 3
σ_{f_i}	Axial stress in the fiber element i, Eq. (4)
σ_{tm_j}	Axial stress in the tensile-matrix element j, Eq. (5)
$\sigma^{\mathrm{peak}}_{\mathrm{tm}_j}$	Peak axial stress in the tensile-matrix element j, Fig. 3
σ_y	Matrix yield stress in tension, Eq. (5)
τ_{sm_k}	Shear stress in the shear-matrix element k, Eq. (13)
τ_y	Matrix yield stress in shear, Eq. (13)
τ^*	Interface threshold stress, Eq. (17)
ζ	Dimensionless co-ordinate parallel to the fibre direction, Eq. (25)

Hedgepeth (1961), and Hedgepeth and Van Dyke (1967). The latter models account for an infinite regular array of elastic fibres carrying tensile load, perfectly bonded to intervening shear carrying elastic matrix. The analytical treatment of shear-lag models becomes difficult if non-linear material responses or deviations from geometric regularity are incorporated.

Much recent effort has been aimed at extending shear-lag models to account for the non-linearities in material response. Although many of these pertain to polymer matrix composites, they contain elements of direct relevance to the metal-matrix composites of present interest. The shear lag model of Beyerlein and Phoenix (1996) extended the classical shear lag model to account for perfectly plastic or sliding matrix material. Using this model, Beyerlein and Phoenix (1996) predicted the stresses around sin-

gle and multiple breaks. Landis and McMeeking (1999), extended the model of Cox (1952) by assuming a matrix obeying the J_2 flow theory. They showed that the interfacial shear stress around an isolated fibre break approaches the matrix and interface constitutive response assumed by Beyerlein and Phoenix (1996) with increasing far-field strain. A three-dimensional shear lag based model for the case of fibres arranged in a hexagonal array is due to Okabe et al. (2001). This model accounts for interface debonding and matrix yielding. Okabe and Takeda (2002) introduced linear hardening into the matrix constitutive response. Most recently, Zhang and Wang (2009) have proposed a model that also accounts for matrix yielding, and interfacial debonding. Their model treats these phenomena as special types of breaks and models their interaction through influence superposition. While the models of Beyerlein and Phoenix (1996); Okabe et al. (2001), and Okabe and Takeda (2002) assume a compliant matrix incapable of carrying tensile loads, the models of Beyerlein and Landis (1999) and Zhang and Wang (2009) allow for non-negligible matrix stiffness as well. Pimenta and Robinson (2014) recently proposed a shear-lag model involving a matrix obeying a non-linear traction-separation law.

The effect of deviation from regular packing on stress concentrations, and ineffective length was studied by Swolfs et al. (2012). In polymer matrix composites, Swolfs et al. (2015) found that matrix cracks have an insignificant effect on composite strength. Mishnaevsky and Brøndsted (2009) studied the stress state produced in a partially damaged realistic microstructure using the finite element method. They also studied the effects of matrix cracking, and interfacial debonding on composite strength.

While most of the aforementioned models – both finite element based, and shear-lag based – are computationally tractable for small clusters of breaks, they are either unable to treat arbitrary damage and non-linear material response, or treat it approximately using linear superposition of break influences. The latter approximation is not justified in general, as the stress and displacement fields in a non-linear material are not superposable. It has, however, been shown to be satisfactory under certain conditions. For instance, errors of only a few percent in the stress concentration were reported from linear superposition by Xia et al. (2001) when the applied load is sufficiently high to produce gross yielding in the matrix. Amongst the shear-lag models, the model of Beyerlein and Phoenix (1996) replaces yielded matrix, or interfacial sliding by a system of shear forces on the neighbouring fibres. This approach is feasible only when the region of matrix yielding or interfacial sliding is known, or can be guessed using symmetry considerations, a priori. A similar restriction also applies to the shear-lag model of Zhang and Wang (2009), wherein, the extent of matrix yielding, and interfacial sliding near a fibre break are assumed a priori.

Spatially resolved elastic strains in a partially damaged Ti-SiC composite have been reported in the literature by Hanan et al. (2003). Their measurements were made using synchrotron X-ray microdiffraction. The microdiffraction technique measures elastic strains only, even in elastoplastically deforming phases, such as the present Ti matrix. This is because the experimental technique is based upon changes in the diffraction pattern with changing lattice spacing, which is, in turn, proportional to the elastic strain. The plastic strain is not resolved, as plastic deformation leaves the lattice spacing nearly unchanged.

A model of the composite specimen of Hanan et al. (2003), accounting for the full length of all their fibres, is presently analysed. The analysis is based on a formulation wherein non-linear governing differential equations accounting for non-linear deformation plasticity of the matrix, tensile stiffness of the matrix and fibre-matrix interfacial slip are incorporated. The formulation incorporates deformation plasticity and shear-lag theory. Loading to 850 MPa, and unloading therefrom are computer simulated, exactly as in the experiment. Barring the fibre-matrix interfacial strength, all material parameters of the constituent phases are taken from the literature. The present model predicts elastic strain profiles near the breaks in excellent agreement with the measurements of Hanan et al. (2003).

The present model and computational methodology are described in Sections 2–7. Model predictions are compared with experimental observations of Hanan et al. (2003) in Section 8. The predicted fields are also discussed. These comparisons suggest the viability of the present model to realistically capture the load distribution due to arbitrarily complex damage in unidirectional metal matrix composites.

2. Model

2.1. Geometry

Fig. 1 shows the elements making up the model composite. Following the classical shear-lag approximation (Cox, 1952), fibres are assumed to be inflexible in all but their axial direction, z. The matrix domain, which physically experiences both axial and shear deformations, is modelled as two distinct types of elements, termed the tensile matrix and shear matrix regions. These are shown separately in Fig. 1. The tensile matrix admits only axial deformation in the z direction, while the shear matrix undergoes only xz shears. This modelling treatment follows Budiansky et al. (1986) and Mahesh et al. (2004). Fibres in the present composite are indexed as f_i, where $i \in \{0, 1, 2, \ldots, n_\mathrm{f} - 1\}$. Periodicity is assumed. Thus, $\mathrm{f}_{n_\mathrm{f}}$ is equivalent to f_0, as shown.

Each fibre in Fig. 1 is abutted by a pair of shear matrix elements, which in turn are surrounded by a pair of tensile matrix elements. A slider element lies at the interface between the fibre and the shear matrix. The deformation of each element depends on those of its neighbours. In order to identify various elements of the model, and their neighbours, a formal notation is presently introduced. As shown in Fig. 2, the shear matrix elements to the right and left of fibre f_i are denoted $\mathrm{sm}_{\mathrm{f}_i}^+$ and $\mathrm{sm}_{\mathrm{f}_i}^-$, respectively. Similarly, the right and left tensile matrix neighbours of fibre i are denoted $\mathrm{tm}_{\mathrm{f}_i}^+$ and $\mathrm{tm}_{\mathrm{f}_i}^-$, respectively, and the right and left slider elements as $\mathrm{s}_{\mathrm{f}_i}^+$ and $\mathrm{s}_{\mathrm{f}_i}^-$, respectively. These neighbouring elements of fibre f_i are labelled on the left in Fig. 2. In an entirely similar manner, the neighbouring elements of tensile matrix tm_j are as shown labelled on the right side of Fig. 2.

Unlike fibre and tensile matrix elements, shear matrix element sm_k is abutted by unique fibre, tensile matrix, and slider elements, denoted by $\mathrm{f}_{\mathrm{sm}_k}$, $\mathrm{tm}_{\mathrm{sm}_k}$, and $\mathrm{s}_{\mathrm{sm}_k}$, respectively. These elements are labelled below in Fig. 2. The same is also true of slider elements: the fibre, tensile matrix, and shear matrix neighbours of slider element s_k are $\mathrm{f}_{\mathrm{s}_k}$, $\mathrm{tm}_{\mathrm{s}_k}$, and $\mathrm{sm}_{\mathrm{s}_k}$, respectively. These elements are not marked in Fig. 2.

2.2. Displacements and strains

Displacement and strain fields evolve over the deformation history. Let the deformation history be discretised into steps, $s \in \{0, 1, 2, \ldots\}$, and let step $s = 0$ correspond to the initial unloaded state. Let $w_{\mathrm{f}_i}^{(s)}(z)$ and $w_{\mathrm{tm}_j}^{(s)}(z)$ denote the axial (z-direction) displacements at step s in fibre f_i and tensile matrix tm_j, respectively. Assuming small deformations, the corresponding axial strains are:

$$\epsilon_{\mathrm{f}_i}^{(s)}(z) = \frac{dw_{\mathrm{f}_i}^{(s)}}{dz}(z), \tag{1}$$

and

$$\epsilon_{\mathrm{tm}_j}^{(s)}(z) = \frac{dw_{\mathrm{tm}_j}^{(s)}}{dz}(z). \tag{2}$$

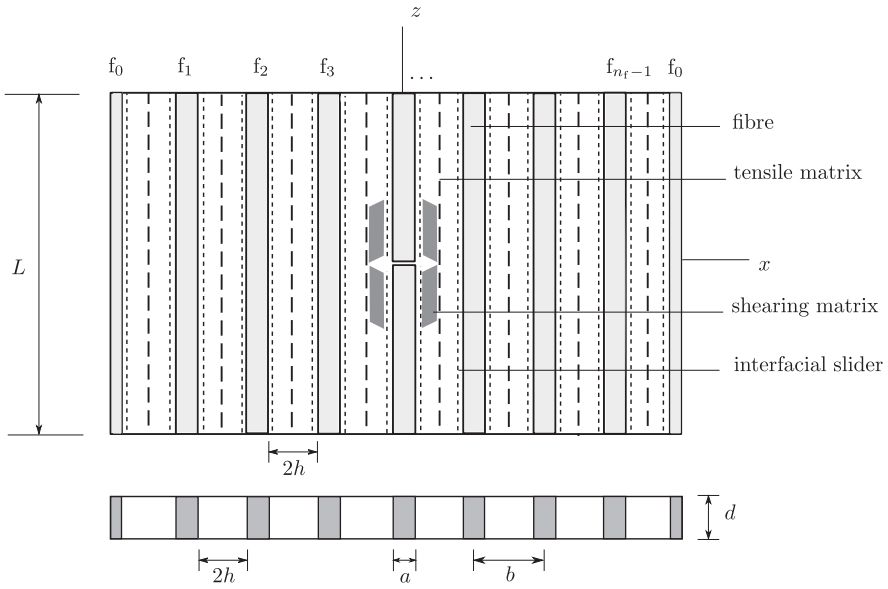

Fig. 1. The model metal matrix composite showing all the model elements. Fibres are shown shaded dark. The matrix domain is divided into two parts: The 'shear matrix' is assumed to deform in simple shear, and the 'tensile matrix' in pure tension. Sliding displacement at the fibre-matrix interface is permitted. A fibre break and matrix shears around it are schematically shown.

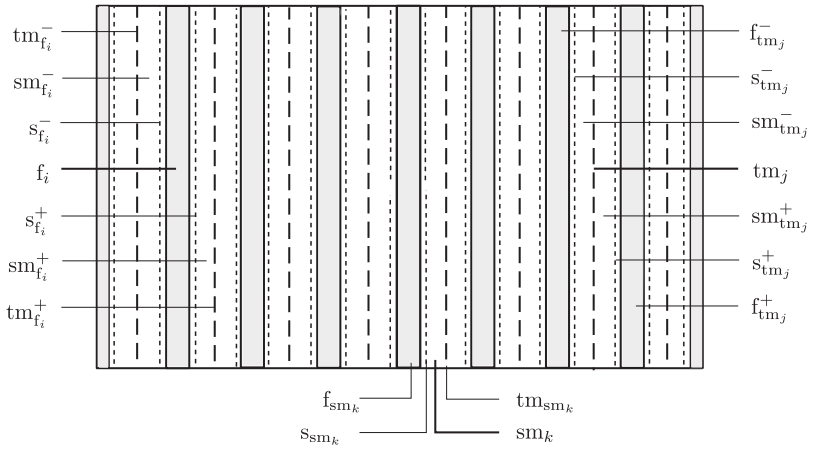

Fig. 2. Model elements neighbouring a typical fibre f_i (labelled on the left side), neighbouring a typical tensile matrix, tm_j (labelled on the right side), and a typical shear matrix sm_k (labelled below).

Let $w^{(s)}_{\mathrm{s}_k}(z)$ denote the displacement in slider s_k. Then, the shear strain in shear matrix sm_k is given by

$$\gamma^{(s)}_{\mathrm{sm}_k}(z) = \left(w^{(s)}_{\mathrm{tm}_{\mathrm{sm}_k}}(z) - w^{(s)}_{\mathrm{f}_{\mathrm{sm}_k}}(z) - w^{(s)}_{\mathrm{s}_{\mathrm{sm}_k}}(z)\right)/h\,. \tag{3}$$

The denominator, $h = (b-a)/2$, is the x-thickness of the shear matrix, which is equal to the distance from the tensile matrix to the surface of a neighbouring fibre. Eqs. (1), and (2) are simply the normal strain-displacement relations corresponding to small strains. The form of the shear strain, given by Eq. (3) follows that of Mahesh et al. (2004).

3. Constitutive assumptions

3.1. Fibre

As in Mahesh et al. (2004), fibres are assumed to remain linear elastic. Let $\sigma_{\mathrm{f}_i}(z)$ denote the stress at coordinate z in fibre element i. Then, neglecting thermal residual strains,

$$\sigma^{(s)}_{\mathrm{f}_i}(z) = E_{\mathrm{f}}\epsilon^{(s)}_{\mathrm{f}_i}(z). \tag{4}$$

3.2. Tensile matrix

The elastoplastic matrix is treated in the deformation theory framework (Jones, 2009). Following Hill (1998), and Mahesh et al. (2004), the stress-strain relationship under monotonic loading from step 0 to step s is taken to follow:

$$\sigma^{(s)}_{\mathrm{tm}_j}(z) = \sigma_{\mathrm{Y}}\tanh\left(\frac{(E_1-E_2)\varepsilon^{(s)}_{\mathrm{tm}_j}(z)}{\sigma_{\mathrm{Y}}}\right) + E_2\varepsilon^{(s)}_{\mathrm{tm}_j}(z). \tag{5}$$

In Eq. (5), E_1, E_2, and σ_{Y} denote the tensile Young's modulus, the hardening modulus of plastic deformation and yield strength of the tensile matrix material, respectively. Eq. (5) is plotted as the monotonically increasing curve in Fig. 3.

The deformation theory stress-strain relationship given in Eq. (5) is adequate for monotonic loading of material points in the matrix. However, even in a tensile specimen that is loaded monotonically at the grips, tensile matrix breakage will cause unloading of the tensile matrix material points in the vicinity of the break. A novel methodology is developed presently to track such unloading. The final result of this development is Eq. (12) below.

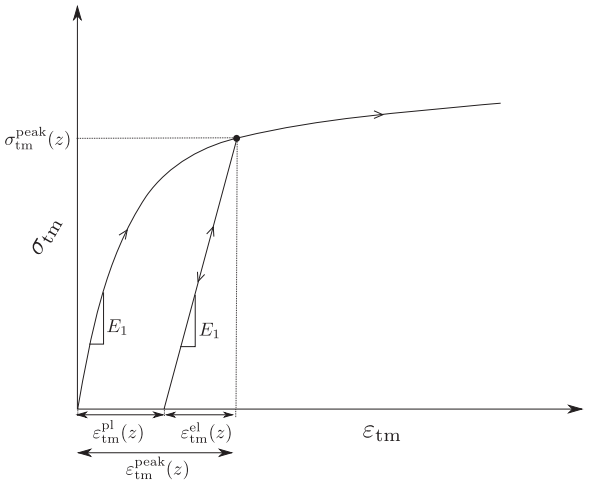

Fig. 3. Stress-strain response of a tensile matrix element during loading and unloading. A plastic set $\varepsilon^{\text{pl}}_{\text{tm}}(z)$ is associated with unloading from the peak stress $\sigma^{\text{peak}}_{\text{tm}}(z)$.

Consider the composite at the end of step S (the 'current state'). An important state variable is the maximum or peak strain experienced by the material point up until the current state:

$$\epsilon^{\text{peak}}_{\text{tm}_j}(z) = \max_{s=0,\ldots,S} \max\left(\epsilon^{(s)}_{\text{tm}_j}(z), 0\right). \tag{6}$$

Here, non-negativity is enforced upon the peak strain in tensile matrix elements. The material point is defined to be 'loading' during step $(S+1)$ if

$$\epsilon^{(S+1)}_{\text{tm}_j}(z) \geq \epsilon^{\text{peak}}_{\text{tm}_j}(z). \tag{7}$$

Otherwise, the material point is said be unloading. As shown in Fig. 3, if unloading occurs from the maximum stress $\sigma^{\text{peak}}_{\text{tm}}(z)$, the tensile matrix element will deform elastically, following:

$$\sigma^{(s)}_{\text{tm}_j}(z) = E_1\left(\varepsilon^{(s)}_{\text{tm}_j}(z) - \varepsilon^{\text{pl}}_{\text{tm}_j}(z)\right). \tag{8}$$

Here, $\varepsilon^{\text{pl}}_{\text{tm}_j}(z)$, the plastic set in the element, is given by

$$\varepsilon^{\text{pl}}_{\text{tm}_j}(z) = \varepsilon^{\text{peak}}_{\text{tm}_j}(z) - \sigma^{\text{peak}}_{\text{tm}_j}(z)/E_1. \tag{9}$$

$\sigma^{\text{peak}}_{\text{tm}_j}$ is the stress that results by substituting $\varepsilon_{\text{tm}_j}(z) = \varepsilon^{\text{peak}}_{\text{tm}_j}(z)$ in Eq. (5).

The loading/unloading history of a tensile matrix element is captured by the internal variables $\varepsilon^{\text{peak}}_{\text{tm}_j}(z)$, and $\varepsilon^{\text{pl}}_{\text{tm}_j}(z)$. The constitutive law for the tensile matrix can be expressed by combining Eqs. (5) and (8) as:

$$\sigma^{(s)}_{\text{tm}_j}(z) = \begin{cases} \sigma_{\text{Y}} \tanh\left(\dfrac{(E_1 - E_2)\varepsilon^{(s)}_{\text{tm}_j}(z)}{\sigma_{\text{Y}}}\right) & \\ \quad + E_2\varepsilon^{(s)}_{\text{tm}_j}(z), & \varepsilon^{(s)}_{\text{tm}_j}(z) \geq \varepsilon^{\text{peak}}_{\text{tm}_j}(z) \\ E_1\left(\varepsilon^{(s)}_{\text{tm}_j}(z) - \varepsilon^{\text{pl}}_{\text{tm}_j}(z)\right), & \varepsilon^{(s)}_{\text{tm}_j}(z) < \varepsilon^{\text{peak}}_{\text{tm}_j}(z). \end{cases} \tag{10}$$

Eq. (10) ensures continuity of $\sigma^{(s)}_{\text{tm}_j}(z)$ with $\epsilon^{(s)}_{\text{tm}_j}(z)$, over an arbitrary loading history, involving arbitrary switches between loading and unloading states. There is, however, a discontinuity in the slope, $(d\sigma^{(s)}_{\text{tm}_j}(z)/d\epsilon^{(s)}_{\text{tm}_j}(z))$ at $\varepsilon^{(s)}_{\text{tm}_j}(z) = \varepsilon^{\text{peak}}_{\text{tm}_j}(z)$. The slope discontinuity is inconducive to application of efficient gradient-based numerical methods. Therefore, a differentiable function that smoothly transitions between loading and unloading states is introduced as follows:

$$\text{I}^{(s)}_{\text{tm}_j}(z) = \frac{1}{2}\left(1 + \tanh\left(\frac{\varepsilon^{(s)}_{\text{tm}_j}(z) - \varepsilon^{\text{peak}}_{\text{tm}_j}(z)}{\varepsilon_{\text{round}}}\right)\right). \tag{11}$$

Here, $\varepsilon_{\text{round}} > 0$ is a smoothing parameter. For $\varepsilon^{(s)}_{\text{tm}_j}(z) \gg \varepsilon^{\text{peak}}_{\text{tm}_j}(z)$ (loading), $\text{I}^{(s)}_{\text{tm}_j}(z) \uparrow 1$. Similarly, for $\varepsilon^{(s)}_{\text{tm}_j}(z) \ll \varepsilon^{\text{peak}}_{\text{tm}_j}(z)$ (unloading), $\text{I}^{(s)}_{\text{tm}_j}(z) \downarrow 0$. The rates of approach increase with decreasing $\varepsilon_{\text{round}}$. In terms of $\text{I}^{(s)}_{\text{tm}_j}(z)$, a differentiable approximation of Eq. (10) is:

$$\sigma^{(s)}_{\text{tm}_j}(z) = \text{I}^{(s)}_{\text{tm}_j}(z)\left(\sigma_{\text{Y}} \tanh\left(\frac{(E_1 - E_2)\varepsilon^{(s)}_{\text{tm}_j}(z)}{\sigma_{\text{Y}}}\right) + E_2\varepsilon^{(s)}_{\text{tm}_j}(z)\right) + (1 - \text{I}^{(s)}_{\text{tm}_j}(z))\left(E_1(\varepsilon^{(s)}_{\text{tm}_j}(z) - \varepsilon^{\text{pl}}_{\text{tm}_j}(z))\right). \tag{12}$$

3.3. Shear matrix

The shear stress-shear strain relationship in the elastoplastic shear matrix can be written, in analogy with Eq. (5), as (Mahesh et al., 2004):

$$\tau^{(s)}_{\text{sm}_k}(z) = \tau_{\text{Y}} \tanh\left(\frac{(E_1 - E_2)\gamma^{(s)}_{\text{sm}_k}(z)}{\tau_{\text{Y}}}\right) + E_2\gamma^{(s)}_{\text{sm}_k}(z). \tag{13}$$

Yielding at a matrix material point strictly depends on both the tensile and shear stress at that point. For simplicity, however, yielding in the tensile matrix and in the shear matrix are assumed to be independent of each other. That is, σ_{Y} and τ_{Y} are assumed independent parameters, as in Zhou et al. (2002).

As with Eq. (5), Eq. (13) is adequate only for monotonic loading. In a composite material with progressive fibre and matrix breakage, the assumption of monotonicity will not be valid. Additionally, the peak and plastic shear strains could be of either sign, in contrast with the peak and plastic tensile strains in the tensile matrix, which can be safely assumed positive (Eq. (6)). To capture the sign, a factor ψ_{sm_k}, is introduced according to the following rules:

(i) If the abutting fibre f_{sm_k} and tensile matrix tm_{sm_k} are both intact, it is assumed that $\gamma^{\text{peak}}_{\text{sm}_k}(z) = \gamma^{\text{pl}}_{\text{sm}_k}(z) = 0$ for all z, and $\psi_{\text{sm}_k} = 0$. That is, the shear matrix bay between a pair of intact tensile elements is assumed not to yield. In Fig. 4, this condition applies to sm_1, sm_2, sm_3, sm_7, sm_{10}, sm_{13}, sm_{14}, sm_{15}, and sm_{16}.

(ii) If the fibre abutting a shear matrix bay, sm_k is broken, and tensile matrix abutting sm_k is intact, it is assumed that $\gamma^{\text{peak}}_{\text{sm}_k}(z) \leq 0$, and $\gamma^{\text{pl}}_{\text{sm}_k}(z) \leq 0$ for all z, and $\psi_{\text{sm}_k} = -1$. In Fig. 4, sm_4, sm_8 and sm_9 are examples of this case.

(iii) If the abutting tensile matrix is broken, but the fibre is intact, $\gamma^{\text{peak}}_{\text{sm}_k}(z) \geq 0$, and $\gamma^{\text{pl}}_{\text{sm}_k}(z) \geq 0$ for all z, and $\psi_{\text{sm}_k} = +1$. Shear matrix bays sm_6, sm_{11}, and sm_{12} are of this type in Fig. 4.

(iv) Finally, if both the abutting fibre and tensile matrix are broken, as in bay sm_5 in Fig. 4, it is assumed that the shear matrix bay will be in a state of unloading. This does not mean that the peak and plastic strains in the shear matrix elements are zero. However, no further evolution of the peak and plastic strains in the shear matrix bay is allowed to occur after the failure of both abutting tensile elements.

In terms of ψ_{sm_k}, the peak shear strain in a shear matrix element is defined, paralleling Eq. (6), as

$$\gamma^{\text{peak}}_{\text{sm}_k}(z) = \psi_{\text{sm}_k} \max_{s=0,\ldots,S} \max(\psi_{\text{sm}_k}\gamma^{(s)}_{\text{sm}_k}(z), 0). \tag{14}$$

A development paralleling that leading up to Eq. (12) yields

$$\tau^{(s)}_{\text{sm}_k}(z) = \text{I}^{(s)}_{\text{sm}_k}(z)\left\{\tau_{\text{Y}} \tanh\left(\frac{(G_1 - G_2)\gamma^{(s)}_{\text{sm}_k}(z)}{\tau_{\text{Y}}}\right) + G_2\gamma^{(s)}_{\text{sm}_k}(z)\right\} + (1 - \text{I}^{(s)}_{\text{sm}_k}(z))\left\{G_1(\gamma^{(s)}_{\text{sm}_k}(z) - \gamma^{\text{pl}}_{\text{sm}_k}(z))\right\}, \tag{15}$$

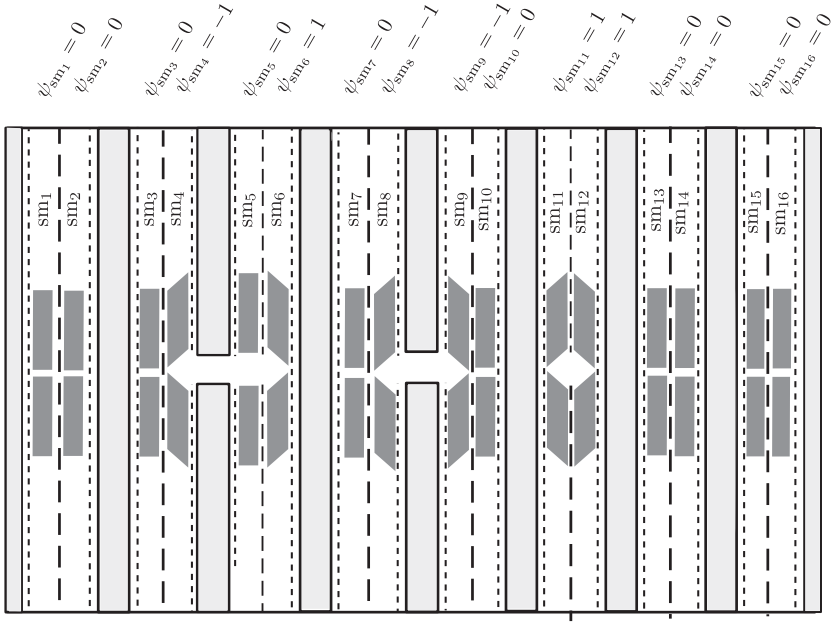

Fig. 4. Schematic representation of the deformed configuration of a partially damaged composite,whose undamaged and undeformed state is shown in Fig. 2. The sign of the maximum and plastic shear strains in shear matrix element k (ψ_{sm_k}) is assumed to depend only on the broken or unbroken state of its abutting fibre and tensile matrix elements, as described in the text.

where,

$$\mathrm{I}^{(s)}_{\mathrm{sm}_k}(z) = \frac{1}{2}\left(1 + \psi_{\mathrm{sm}_k}\tanh\left(\frac{\gamma^{(s)}_{\mathrm{sm}_k}(z) - \gamma^{\mathrm{peak}}_{\mathrm{sm}_k}(z) + \psi_{\mathrm{sm}_k}\gamma_{\mathrm{shift}}}{\gamma_{\mathrm{round}}}\right)\right). \tag{16}$$

The term $\psi_{\mathrm{sm}_k}\gamma_{\mathrm{shift}}$, which appears in Eq. (16) has no analogue in Eq. (11). It is introduced here to ensure that $\mathrm{I}^{(s)}_{\mathrm{sm}_k}(z)$ is strictly monotonic for any $\psi_{\mathrm{sm}_k} \in \{-1, 0, 1\}$.

3.4. Slider elements

A simple threshold slip model is assumed at the fibre-matrix interface, akin to that in Mahesh et al. (2004). The displacement $w^{(s)}_{\mathrm{s}_k}(z)$ in step s of slider element s_k is taken to follow

$$w^{(s)}_{\mathrm{s}_k}(z)\begin{cases} \le 0, & \text{if } \tau^{(s)}_{\mathrm{sm}_{\mathrm{s}_k}}(z) < -\tau^*, \\ = 0, & \text{if } -\tau^* \le \tau^{(s)}_{\mathrm{sm}_{\mathrm{s}_k}}(z) \le \tau^*, \\ \ge 0, & \text{if } \tau^{(s)}_{\mathrm{sm}_{\mathrm{s}_k}}(z) > \tau^*. \end{cases} \tag{17}$$

In the above equation, τ^* is a material constant that describes the interfacial interactions between the fibre and the matrix. The value of $w_{\mathrm{s}_k}(z)$ in the first and third cases is left unspecified. A smooth regularisation of Eq. (17) is given by

$$w^{(s)}_{\mathrm{s}_k}(z) = w_{\mathrm{s}0}\left(\frac{\tau^{(s)}_{\mathrm{sm}_{\mathrm{s}_k}}(z)}{\tau^*}\right)^{2n+1}. \tag{18}$$

Here, $w_{\mathrm{s}0}$ is a reference value for the interfacial sliding displacement. n is to be a sufficiently large positive integer, so that $2n+1$ is odd. This regularisation is a simpler version of that used by Mahesh et al. (2004).

It is emphasised that according to Eq. (18), the sliding displacements are history-independent. The sliding displacement at a given step depends only on the shear stresses in that step.

4. Governing equations and boundary conditions

Following the classical shear-lag framework (Hedgepeth, 1961; Budiansky et al., 1986; Mahesh et al., 2004), the z-equilibrium of fibre element f_i, at step s is expressed as:

$$ad\frac{d\sigma^{(s)}_{\mathrm{f}_i}}{dz}(z) + d\left(\tau^{(s)}_{\mathrm{sm}^+_{\mathrm{f}_i}}(z) + \tau^{(s)}_{\mathrm{sm}^-_{\mathrm{f}_i}}(z)\right) = 0. \tag{19}$$

As shown in Fig. 1, $A_{\mathrm{f}} = ad$ is the fibre cross-sectional area, and d is the ply thickness. Similarly, the z-equilibrium of an infinitesimal tensile matrix element in tm_j can be expressed as

$$d(b-a)\frac{d\sigma^{(s)}_{\mathrm{tm}_j}}{dz}(z) - d\left(\tau^{(s)}_{\mathrm{sm}^+_{\mathrm{tm}_j}}(z) + \tau^{(s)}_{\mathrm{sm}^-_{\mathrm{tm}_j}}(z)\right) = 0. \tag{20}$$

The sliding displacement $w_{\mathrm{s}_k}(z)$ at the fibre-matrix interface is governed by Eq. (18).

The normal and shear stresses appearing in Eqs. (18)–(20) can be expressed in terms of fibre, tensile matrix and slider displacements, $w^{(s)}_{\mathrm{f}_i}(z)$, $w^{(s)}_{\mathrm{tm}_j}(z)$, and $w^{(s)}_{\mathrm{s}_k}(z)$, respectively, using the constitutive laws of Section 3. These displacement fields constitute the unknown variables of the present model.

Breaks in the fibres and tensile matrix elements are assumed to occur in a single plane, taken without loss of generality as the plane $z = 0$, transverse to the fibre direction. The boundary conditions imposed in this plane are

$$\begin{aligned} &\frac{dw^{(s)}_{\mathrm{f}_i}}{dz}(z=0) = 0, \quad \text{if } \mathrm{f}_i \text{ is broken, and} \\ &w^{(s)}_{\mathrm{f}_i}(z=0) = 0, \quad \text{if } \mathrm{f}_i \text{ is intact.} \end{aligned} \tag{21}$$

In tensile matrix tm_j,

$$\begin{aligned} &\left(\frac{dw^{(s)}_{\mathrm{tm}_j}}{dz} - \varepsilon^{\mathrm{pl}}_{\mathrm{tm}_j}\right)(z=0) = 0, \quad \text{if } \mathrm{tm}_j \text{ is broken, and} \\ &w^{(s)}_{\mathrm{tm}_j}(z=0) = 0, \quad \text{if } \mathrm{tm}_j \text{ is intact.} \end{aligned} \tag{22}$$

Because of symmetry, it is sufficient to treat only half the composite domain, $0 \le z \le (L/2)$, shown in Fig. 1. Displacement controlled loading is imposed:

$$w^{(s)}_{\mathrm{f}_i}(z = L/2) = w^{(s)}_{\mathrm{tm}_j}(z = L/2) = L\varepsilon_{\mathrm{engg}}/2. \tag{23}$$

Here, ε_{engg} is the engineering strain imposed over the gauge length.

The tensile load, P, applied to the composite for a given ε_{engg} can be obtained by summing over the tensile loads of the fibres and tensile matrix elements. This sum must be equal at any section, z.

$$P = ad\sum_{i=0}^{n_f-1} E_f \frac{dw_{f_i}^{(s)}}{dz}(z) + 2ah\sum_{j=0}^{n_{tm}-1} \times\left[\left(I_{tm_j}^{(s)}(z)\right)\left\{\sigma_Y \tanh\left(\frac{E_1-E_2}{\sigma_Y}\frac{dw_{tm_j}^{(s)}}{dz}(z)\right)+E_2\frac{dw_{tm_j}^{(s)}}{dz}(z)\right\} + \left(1-I_{tm_j}^{(s)}(z)\right)\left\{E_1\left(\frac{dw_{tm_j}^{(s)}}{dz}(z)-\varepsilon_{tm_j}^{pl}(z)\right)\right\}\right]. \quad (24)$$

Although the equilibrium equations, and boundary conditions, given above are classical, the complex non-linear constitutive laws of the matrix phase, and interface, render these equations not amenable to analytical solution.

5. Non-dimensional equations

Direct numerical solution of the system of equations derived in Section 4 produces significant round-off errors, as the various terms in the governing equations are not of the same order of magnitude. It is therefore desirable to non-dimensionalise these equations with the aim of getting order of unity terms in the latter form. The following novel non-dimensionalisation scheme is developed for this purpose.

First, the axial coordinate z is non-dimensionalised as

$$\zeta = \sqrt{K}z, \quad (25)$$

where,

$$K = \frac{G_1}{\sqrt{2h^3 dE_f E_1}}. \quad (26)$$

The inverse square root of K defines the characteristic length of load recovery the model composite, provided all constituents are elastic. Let the axial displacements of the various model elements be normalised by

$$\hat{w}_{f_i}^{(s)} = Ww_{f_i}^{(s)}, \quad \hat{w}_{tm_j}^{(s)} = Ww_{tm_j}^{(s)}, \text{ and } \quad \hat{w}_{s_k}^{(s)} = Ww_{s_k}^{(s)}. \quad (28)$$

Furthermore, let

$$C = \frac{G_2}{G_1-G_2}$$
$$A = (1+C)\sqrt{\frac{d}{2h}\frac{E_f}{E_1}},$$
$$B = 2(1+C)h^2K\frac{E_1}{G_1},$$
$$E = \frac{\tau_Y}{\sigma_Y}\frac{(E_1-E_2)}{(G_1-G_2)}\frac{h}{\sqrt{K}},$$
$$F = \frac{1}{(1+C)}\frac{G_1}{E_1}\frac{\sigma_Y}{\tau_Y}\frac{1}{h\sqrt{K}},$$
$$H = \frac{E_2}{E_1}, \text{ and}$$
$$I = \frac{\tau^*}{\tau_Y}. \quad (29)$$

The parameters listed in Eq. (29) are dimensionless and of the order of unity. In terms of these variables, the normalised governing equations take the following simpler forms. Eq. (19), describing fibre equilibrium, expressed in terms of the normalised fibre, tensile matrix, and slider displacements becomes

$$A\frac{d^2\hat{w}_{f_i}^{(s)}}{d\zeta^2}(\zeta) + \left\{I_{sm_{f_i}^+}^{(s)}(\zeta)\tanh\left(\hat{w}_{tm_{f_i}^+}^{(s)}(\zeta)-\hat{w}_{f_i}^{(s)}(\zeta)-\hat{w}_{s_{f_i}^+}^{(s)}(\zeta)\right) + I_{sm_{f_i}^-}^{(s)}(\zeta)\tanh\left(\hat{w}_{tm_{f_i}^-}^{(s)}(\zeta)-\hat{w}_{f_i}^{(s)}(\zeta)-\hat{w}_{s_{f_i}^-}^{(s)}(\zeta)\right)\right\} + C\left\{I_{sm_{f_i}^+}^{(s)}(\zeta)\left(\hat{w}_{tm_{f_i}^+}^{(s)}(\zeta)-\hat{w}_{f_i}^{(s)}(\zeta)-\hat{w}_{s_{f_i}^+}^{(s)}(\zeta)\right) + I_{sm_{f_i}^-}^{(s)}(\zeta)\left(\hat{w}_{tm_{f_i}^-}^{(s)}(\zeta)-\hat{w}_{f_i}^{(s)}(\zeta)-\hat{w}_{s_{f_i}^-}^{(s)}(\zeta)\right)\right\} + (1+C) \times\left\{\left(1-I_{sm_{f_i}^+}^{(s)}(\zeta)\right)\left(\hat{w}_{tm_{f_i}^+}^{(s)}(\zeta)-\hat{w}_{f_i}^{(s)}(\zeta)-\hat{w}_{s_{f_i}^+}^{(s)}(\zeta)-\hat{\gamma}_{sm_{f_i}^+}^{pl}(\zeta)\right) + \left(1-I_{sm_{f_i}^-}^{(s)}(\zeta)\right)\left(\hat{w}_{tm_{f_i}^-}^{(s)}(\zeta)-\hat{w}_{f_i}^{(s)}(\zeta)-\hat{w}_{s_{f_i}^-}^{(s)}(\zeta)-\hat{\gamma}_{sm_{f_i}^-}^{pl}(\zeta)\right)\right\}=0. \quad (30)$$

In this expression, the normalised shear matrix plastic strain is defined as

$$\hat{\gamma}_{sm_k}^{pl} = \frac{\left(\hat{w}_{tm_{sm_k}}^{(s)}-\hat{w}_{f_{sm_k}}^{(s)}-\hat{w}_{s_{sm_k}}^{(s)}\right)-\tanh\left(\hat{w}_{tm_{sm_k}}^{(s)}-\hat{w}_{f_{sm_k}}^{(s)}-\hat{w}_{s_{sm_k}}^{(s)}\right)}{1+C}. \quad (31)$$

Similarly, Eq. (20) transforms to

$$I_{tm_j}^{(s)}(\zeta)B\frac{d^2\hat{w}_{tm_j}^{(s)}}{d\zeta^2}(\zeta)\left\{H+(1-H)\operatorname{sech}^2\left(E\frac{d\hat{w}_{tm_j}^{(s)}(\zeta)}{d\zeta}\right)\right\} - \left\{I_{sm_{tm_j}^+}^{(s)}(\zeta)\tanh\left(\hat{w}_{tm_j}^{(s)}(\zeta)-\hat{w}_{f_{tm_j}^+}^{(s)}(\zeta)-\hat{w}_{s_{tm_j}^+}^{(s)}(\zeta)\right) + I_{sm_{tm_j}^-}^{(s)}(\zeta)\tanh\left(\hat{w}_{tm_j}^{(s)}(\zeta)-\hat{w}_{f_{tm_j}^-}^{(s)}(\zeta)-\hat{w}_{s_{tm_j}^-}^{(s)}(\zeta)\right)\right\} - C\left\{I_{sm_{tm_j}^+}^{(s)}(\zeta)\left(\hat{w}_{tm_j}^{(s)}(\zeta)-\hat{w}_{f_{tm_j}^+}^{(s)}(\zeta)-\hat{w}_{s_{tm_j}^+}^{(s)}(\zeta)\right) + .I_{sm_{tm_j}^-}^{(s)}(\zeta)\left(\hat{w}_{tm_j}^{(s)}(\zeta)-\hat{w}_{f_{tm_j}^-}^{(s)}(\zeta)-\hat{w}_{s_{tm_j}^-}^{(s)}(\zeta)\right)\right\} + B\left(1-I_{tm_j}^{(s)}(\zeta)\right)\left(\frac{d^2\hat{w}_{tm_j}^{(s)}(\zeta)}{d\zeta^2}-\frac{d\hat{\varepsilon}_{tm_j}^{pl}(\zeta)}{d\zeta}\right) - (1+C) \times\left\{\left(1-I_{sm_{tm_j}^+}^{(s)}(\zeta)\right)\left(\hat{w}_{tm_j}^{(s)}(\zeta)-\hat{w}_{f_{tm_j}^+}^{(s)}(\zeta)-\hat{w}_{s_{tm_j}^+}^{(s)}(\zeta)-\hat{\gamma}_{sm_{tm_j}^+}^{pl}(\zeta)\right) + \left(1-I_{sm_{tm_j}^-}^{(s)}(\zeta)\right) \times\left(\hat{w}_{tm_j}^{(s)}(\zeta)-\hat{w}_{f_{tm_j}^-}^{(s)}(\zeta)-\hat{w}_{s_{tm_j}^-}^{(s)}(\zeta)-\hat{\gamma}_{sm_{tm_j}^-}^{pl}(\zeta)\right)\right\}=0. \quad (32)$$

In this expression,

$$\hat{\varepsilon}_{tm_j}^{pl} = (1-H)\frac{d\hat{w}_{tm_j}^{(s)}}{d\zeta} - F\tanh\left(E\frac{d\hat{w}_{tm_j}^{(s)}}{d\zeta}\right). \quad (33)$$

Finally, the slider constitutive law, Eq. (18), becomes

$$\hat{w}_{s_{s_k}}^{(s)}(\zeta) - \left\{\frac{1}{I}\left\{I_{sm_{s_k}}^{(s)}(\zeta)\left(\tanh\left(\hat{w}_{tm_{s_k}}^{(s)}(\zeta)-\hat{w}_{f_{s_k}}^{(s)}(\zeta)-\hat{w}_{s_{s_k}}^{(s)}(\zeta)\right)\right.\right. + \left.\left. C\left(\hat{w}_{tm_{s_k}}^{(s)}(\zeta)-\hat{w}_{f_{s_k}}^{(s)}(\zeta)-\hat{w}_{tm_{s_k}}^{(s)}(\zeta)\right)\right)\right.$$

$$+(1-\mathrm{I}^{(s)}_{\mathrm{sm}_{s_k}}(\zeta))(1+C)$$
$$\times\left(\hat{w}^{(s)}_{\mathrm{tm}_{s_k}}(\zeta)-\hat{w}^{(s)}_{\mathrm{f}_{s_k}}(\zeta)-\hat{w}^{(s)}_{\mathrm{s}_{s_k}}(\zeta)-\hat{\gamma}^{\mathrm{pl}}_{s_k}(\zeta)\right)\Big\}\Big\}^{2n+1}=0. \quad (34)$$

The normalised form of boundary conditions Eqs. (21), and (22) become,

$$\frac{d\hat{w}^{(s)}_{\mathrm{f}_i}}{d\zeta}(\zeta=0)=0, \quad \text{if } \mathrm{f}_i \text{ is broken, and}$$
$$\hat{w}^{(s)}_{\mathrm{f}_i}(\zeta=0)=0, \quad \text{if } \mathrm{f}_i \text{ is intact.} \quad (35)$$

Similarly, in tensile matrix tm_j,

$$\left(\frac{d\hat{w}^{(s)}_{\mathrm{tm}_j}}{d\zeta}-\hat{\varepsilon}^{\mathrm{pl}}_{\mathrm{tm}_j}\right)(\zeta=0)=0, \quad \text{if } \mathrm{tm}_j \text{ is broken, and}$$
$$\hat{w}^{(s)}_{\mathrm{tm}_j}(\zeta=0)=0, \quad \text{if } \mathrm{tm}_j \text{ is intact.} \quad (36)$$

Finally, the imposed displacement can be normalised as

$$\hat{w}^{(s)}_{\mathrm{f}_i}(\zeta=\ell)=\hat{w}^{(s)}_{\mathrm{tm}_j}(\zeta=\ell)=W(L\varepsilon_{\mathrm{engg}}/2), \quad (37)$$

where $\ell=\sqrt{K}L/2$. Thus, the system of equations, Eqs. (30), (32), and (34) and boundary conditions Eqs. (35)–(37) describe the present composite material, in terms of seven independent non-dimensional constants listed in Eq. (29).

The total load imposed upon the composite is given by Eq. (24). The non-dimensional total load is defined as

$$\hat{P}=P\Big/\left(\frac{E_{\mathrm{f}}}{G_1-G_2}h\sqrt{K}a^2\tau_{\mathrm{Y}}\right), \quad (38)$$

where,

$$\hat{P}(\zeta)=\sum_{i=0}^{n_{\mathrm{f}}-1}\frac{d\hat{w}^{(s)}_{\mathrm{f}_i}}{d\zeta}(\zeta)+\left(\frac{1+C}{A}\right)^2\sum_{j=0}^{n_{\mathrm{tm}}-1}$$
$$\times\left[\mathrm{I}^{(s)}_{\mathrm{tm}_j}(\zeta)\left\{\frac{1-H}{E}\tanh\left(E\frac{d\hat{w}^{(s)}_{\mathrm{tm}_j}}{d\zeta}(\zeta)\right)+H\frac{d\hat{w}^{(s)}_{\mathrm{tm}_j}}{dz}(\zeta)\right\}\right.$$
$$\left.+\left(1-\mathrm{I}^{(s)}_{\mathrm{tm}_j}(\zeta)\right)\left\{E_1\left(\frac{d\hat{w}^{(s)}_{\mathrm{tm}_j}}{d\zeta}(\zeta)-\hat{\varepsilon}^{\mathrm{pl}}_{\mathrm{tm}_j}(\zeta)\right)\right\}\right]. \quad (39)$$

For equilibrium, the total load should be conserved across cross-sections. Therefore, the above expression should yield the same $\hat{P}$ for all $\zeta\in[0,\ell]$.

6. Reduced linear model

The mechanical fields predicted by the present model, which accounts for matrix plasticity, and interfacial sliding vary non-linearly with applied composite stress σ_c. It will prove insightful to compare the predictions with those of a reduced linear model, which accounts for fibre and matrix stiffness, but not for matrix plasticity, nor for interfacial sliding. The reduced linear problem is governed by the equations

$$A\frac{d^2\hat{w}^{(s)}_{\mathrm{f}_i}(\zeta)}{d\zeta^2}+(1+C)$$
$$\times\left\{\left(\hat{w}^{(s)}_{\mathrm{tm}^+_{\mathrm{f}_i}}(\zeta)-\hat{w}^{(s)}_{\mathrm{f}_i}(\zeta)\right)+\left(\hat{w}^{(s)}_{\mathrm{tm}^-_{\mathrm{f}_i}}(\zeta)-\hat{w}^{(s)}_{\mathrm{f}_i}(\zeta)\right)\right\}=0 \quad (40)$$

for the fibre, and

$$B\frac{d^2\hat{w}^{(s)}_{\mathrm{tm}_j}(\zeta)}{d\zeta^2}-(1+C)$$
$$\times\left\{\left(\hat{w}^{(s)}_{\mathrm{tm}_j}(\zeta)-\hat{w}^{(s)}_{\mathrm{f}^+_{\mathrm{tm}_j}}(\zeta)\right)+\left(\hat{w}^{(s)}_{\mathrm{tm}_j}(\zeta)-\hat{w}^{(s)}_{\mathrm{f}^-_{\mathrm{tm}_j}}(\zeta)\right)\right\}=0 \quad (41)$$

for the matrix. The fibre boundary conditions remain those given by Eq. (35), while the matrix boundary conditions become

$$\frac{d\hat{w}^{(s)}_{\mathrm{tm}_j}}{d\zeta}(\zeta=0)=0, \quad \text{if } \mathrm{tm}_j \text{ is broken, and}$$
$$\hat{w}^{(s)}_{\mathrm{tm}_j}(\zeta=0)=0, \quad \text{if } \mathrm{tm}_j \text{ is intact.} \quad (42)$$

The loading boundary conditions remain the same as Eq. (37).

7. Numerical solution

Numerical solution of the present system of equations using the finite difference method applied over a uniform grid along the ζ-direction was found infeasible. This is partly because of the well known Runge phenomenon associated with the uniform grid (Trefethen, 2013), and partly also because the exponential load recovery profiles near fibre breaks require a very high order approximation of derivatives to resolve sufficiently accurately. These issues are avoided presently through the use of the pseudospectral collocation method (Fornberg, 1998a) over a Chebyshev grid:

$$\zeta_\iota=\ell\left(1-\cos\left(\frac{\pi\iota}{n_C-1}\right)\right), \qquad \iota=0,1,2,\ldots,n_C-1. \quad (43)$$

Here, n_C is the number of Chebyshev points. The ζ_ι grid is quadratically clustered near the ends of the domain in order to suppress the Runge phenomenon. All axial elements – fibres, tensile matrices, and sliders – are discretised by placing regular nodes at the grid points. Eqs. (30) – (34) are enforced in discretised form at the regular nodes. In doing so, the differential operators are discretised using differentiation matrices (Fornberg, 1998a; Weideman and Reddy, 2000). Let $\{\hat{w}_{\mathrm{f}_i}\}$ denote the vector of normalised displacements at positions ζ_ι in fibre f_i. Then, p-th order dense differentiation matrices $[D^{(p)}]$ are constructed, following the procedure given by Fornberg (1998b), which accurately approximate the axial derivatives:

$$\frac{d^{(p)}\{\hat{w}_{\mathrm{f}_i}\}}{d\zeta^{(p)}}=[D^{(p)}]\{\hat{w}_{\mathrm{f}_i}\}. \quad (44)$$

Similarly, if $\{\hat{w}_{\mathrm{tm}_j}\}$ denotes the vector of normalised displacements in the tensile matrix element tm_i,

$$\frac{d^{(p)}\{\hat{w}_{\mathrm{tm}_j}\}}{d\zeta^{(p)}}=[D^{(p)}]\{\hat{w}_{\mathrm{tm}_j}\}. \quad (45)$$

The governing equation for the slider elements is purely algebraic, and hence does not need any treatment of derivatives.

Fictitious nodes corresponding to $\iota=-1$ and $\iota=n_C$ are introduced in the fibre and tensile matrix axial elements. The former node can be located at any arbitrary ζ such that $\zeta<0$, and the latter node at any ζ such that $\zeta>\ell$, as shown by Fornberg (1998b). These fictitious nodes are used to enforce the boundary conditions.

The discretised equations are non-linear. Their iterative solution is accomplished using a standard solver, MINPACK (Moré et al., 1980). The determination of the Jacobian matrix for the system of equations proves to be tedious, but straightforward.

In addition to the desirable numerical characteristics noted above, pseudospectal collocation has exponential convergence rates, much faster than the power-law convergence rates of the finite element or finite difference methods (Weideman and Reddy, 2000). The additional speed comes at the cost of dense interaction matrices, and hence greater demand for computer memory.

Composite loading/unloading history can be simulated over a number of steps. A number of iterations are performed within each step. Following the standard procedure of plasticity simulations (Simo and Hughes, 2006), each iteration involves progressing toward global equilibrium, i.e., a reduction of the residuals corresponding to Eqs. (30) and (32). This step is performed keeping

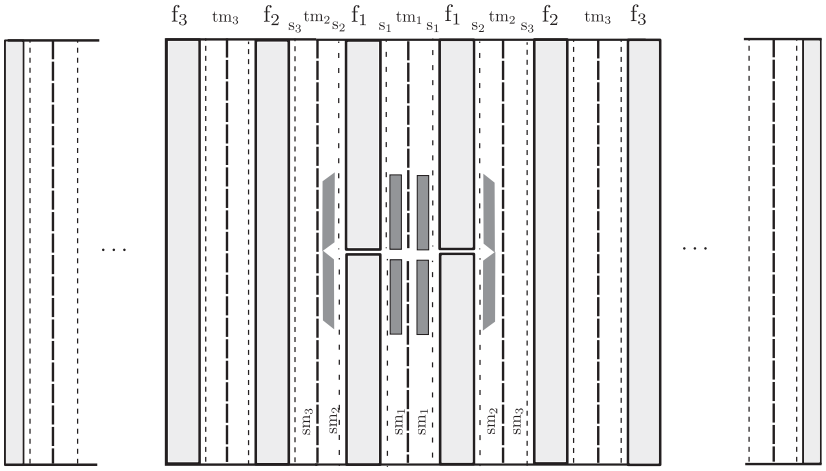

Fig. 5. Broken and intact fibres in the metal matrix composite of Hanan et al. (2003) showing the nomenclature of model elements.

all the internal variables of the model fixed. Sliding displacements $\hat{w}_{s_k}$ are updated after each iteration so that Eq. (34) is satisfied after each equilibrium iteration. Iterations are terminated when all the governing equations and boundary conditions in Section 5 are satisfied to a tight tolerance. At this point, the peak and plastic strains in the matrix elements are updated, and the next step is commenced.

8. Results

8.1. Comparison with experimental results

Using synchrotron X-ray micro-diffraction, Hanan et al. (2003) measured the stress redistribution in a damaged commercial Ti matrix composite laminate (SiC fibres in a Ti-6Al-4V matrix). It is recalled from Section 1 that X-ray micro-diffraction resolves only the elastic part of strain, even in an elasoplatically deforming material. Hanan et al. (2003) introduced a fibre break by drilling a circular hole with electric discharge machining. The hole fully cut one fibre, and one of its adjoining matrix bays. It was also suspected to have partially broken the next fibre. This partial damage led to the breakage of the neighbouring fibre during loading. At the moment of measuring elastic strains, Hanan et al. (2003) report that two adjacent fibres and the intervening matrix were broken. These breaks were approximately all located in a plane transverse to the fibre direction. Fig. 5 shows a schematic diagram of the system of breaks and the naming scheme for the various axial model elements that are either broken, or in the vicinity of the broken elements. In this scheme, the two symmetrically broken fibres are denoted f_1, the broken tensile matrix element is denoted tm_1, etc. It is assumed that the process of hole-drilling would relax all residual stresses in the composite, at least in the vicinity of the hole. For this reason, and for simplicity, the present study assumes zero axial thermal residual stresses throughout the model domain.

Exploiting symmetry, only half the specimen of Hanan et al. (2003), $0\,\text{mm} \le z \le 13\,\text{mm}$, is modelled. The model domain, however, includes all the 29 fibres in the experimental specimen, and has an axial extent in the fibre direction of $l = 13$ mm, which is the actual half-length of the experimental specimen. Even so, the present computation, which in involves loading up to 850 MPa in one step, and unloading to 0 MPa in one step, requires only about 23 seconds of wall-clock computer time.

The important cross-sectional dimensions in the composite of Hanan et al. (2003) are shown in Fig. 6a. In the present model, fibres are idealised to have square cross-sections, with side dimension a, as shown in Fig. 6b, and ply thickness $d = a$. The dimension, a, is determined such that the fibre cross-sectional area $A_f = a^2 = \pi\,(140\ \mu\text{m})^2/4$. Also, the centre-to-centre spacing of fibres, $b = 240\ \mu$m is preserved in the course of the idealisation. These choices make the volume fraction of fibres in the actual ply somewhat smaller than that in the idealised ply.

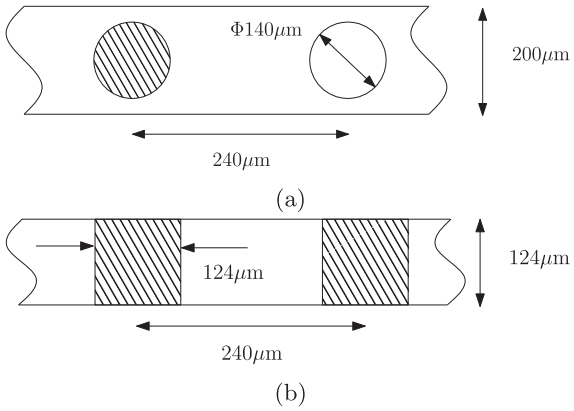

Fig. 6. (a) Actual (Hanan et al., 2003), and (b) idealised *xy* cross-sections of the one ply composite. Fibre cross-sectional area, A_f, and the fibre centre-to-centre spacing are preserved in the course of the idealisation.

Table 1
Geometric and material parameters of the present model.

Parameter	Value	Reference
Fiber dimension, a	124 μm	Hanan et al. (2003)
Fibre spacing, b	240 μm	Hanan et al. (2003)
Ply thickness, d	124 μm	Hanan et al. (2003)
Composite half-length, l	13 mm	Hanan et al. (2003)
Fiber elastic modulus, E_f	400 GPa	Wessel (2004)
Matrix elastic tensile modulus, E_1	110 GPa	Welsch et al. (1993)
Matrix plastic tensile hardening, E_2	1.25 GPa	Ziaja (2009)
Matrix elastic shear modulus, G_1	42 GPa	Welsch et al. (1993)
Matrix plastic shear modulus, G_2	0.5 GPa	assuming $G_2/G_1 = E_2/E_1$
Matrix tensile yield stress σ_Y	820 MPa	Welsch et al. (1993)
Matrix shear yield stress τ_Y	550 MPa	Welsch et al. (1993)
Interfacial strength, τ^*	270 MPa	present work
n	4	computational parameter
$\varepsilon_{\text{round}}$	0.5	computational parameter
γ_{round}	1.0	computational parameter
γ_{shift}	1.3	computational parameter

The material properties of the fibre, and matrix are obtained from the literature, as listed in Table 1. n, $\varepsilon_{\text{round}}$, γ_{round}, and γ_{shift}

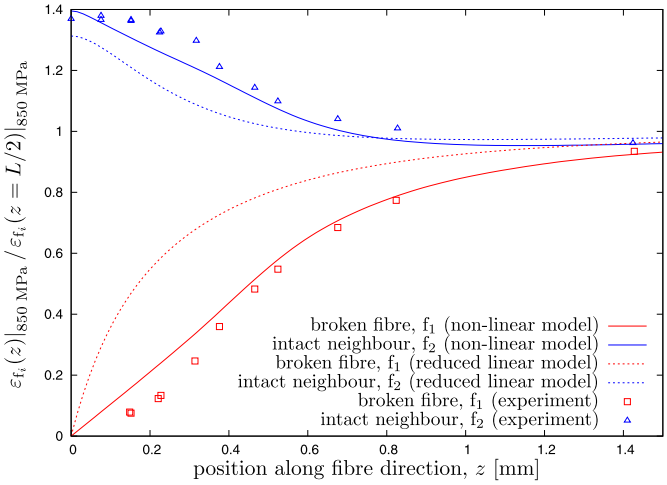

Fig. 7. Strain concentration predicted in the fibres by the model after loading to 850 MPa (solid lines), compared with the experimental data (points) reported by Hanan et al. (2003). Fibres f_1 and f_2 are identified with respect to the broken elements in Fig. 5.

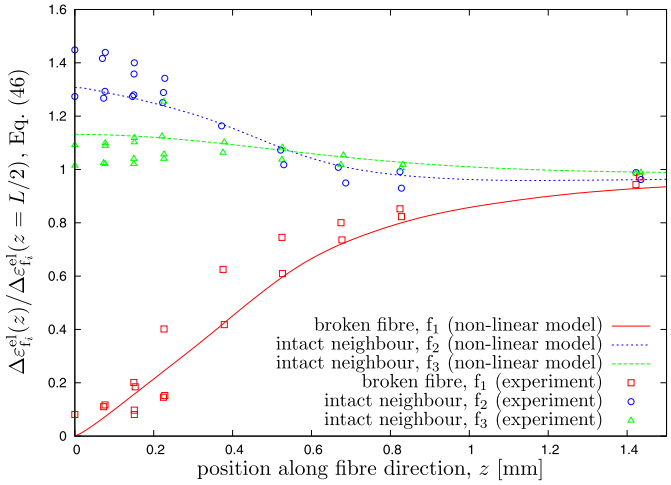

Fig. 8. Change in the fibre elastic strains between the loaded and unloaded states. Predictions from the present model are compared with experimental data points taken from Figs. 8 and 9 of Hanan et al. (2003).

represent numerical smoothing parameter, and not material constants to be fit. Model predictions are not sensitive to their values, so long as they are sufficiently large. The hardening rate of the yielded matrix in shear, G_2 is assigned a value assuming $G_2/G_1 = E_2/E_1$. However, the interfacial shear strength, τ^*, is treated as a present fitting parameter. Its value is fit to $\tau^* = 270$ MPa, so that the presently predicted load recovery near a cluster of breaks matches that experimentally measured by Hanan et al. (2003). This value is considerably larger than the typical values of 90–200 MPa obtained from push-out tests, conventional full fragmentation testing, or synchrotron strain measurements (Preuss et al., 2002).

The loaded strain measurements were made by Hanan et al. (2003) at a far-field stress of 850 MPa. This corresponds to $P = 850\ \text{MPa} \times 7\ \text{mm} \times 0.2\ \text{mm} \approx 1190$ N in Eq. (24). By successive bisection, the model displacement at $z = L/2$ is determined such that the model load matches the experimental load. This condition is realised at $w_{f_i}(z = L/2) = w_{tm_j}(z = L/2) \approx 0.07$ mm, for all i, j or $\varepsilon_{engg} \approx 0.005$.

Elastic strains are predicted by the present model in the broken fibres, and in an intact fibre neighbouring either of the broken ones. These predictions are compared in Fig. 7 with the experimental measurements of Hanan et al. (2003). The simulated elastic strain profiles broadly agree with the measured profiles in both fibres f_1 and f_2. The strain variations predicted by the reduced linear model (Section 6) are also shown in Fig. 7. It is clear that the latter model predicts a more rapid load recovery profile than the non-linear model in the broken fibre. This shows that the non-linear phenomena, viz., matrix yielding, and interfacial sliding, modelled presently play an important role in determining the near-break mechanical fields.

Systematic differences between the predicted and measured strains are, however, observed. Over $0\,\text{mm} \le z \le 0.5\,\text{mm}$, the strains predicted in the broken fibres are in excess of the measurements. Over the same range of z, the strains are somewhat underpredicted in the next intact fibre, f_2. For $0.5\,\text{mm} \le z \le 1.4\,\text{mm}$, the agreement between predictions and experiment is better. The error bars reported by Hanan et al. (2003) for the fibre strain measurements are too small to account for the observed discrepancy in $0\,\text{mm} \le z \le 0.5\,\text{mm}$. A plausible explanation is that the assumption of a uniform interfacial strength τ^* may not be obeyed in the physical specimen. Sizeable variation in τ^* near the fibre breaks may underlie the observed discrepancies in the fibre strains.

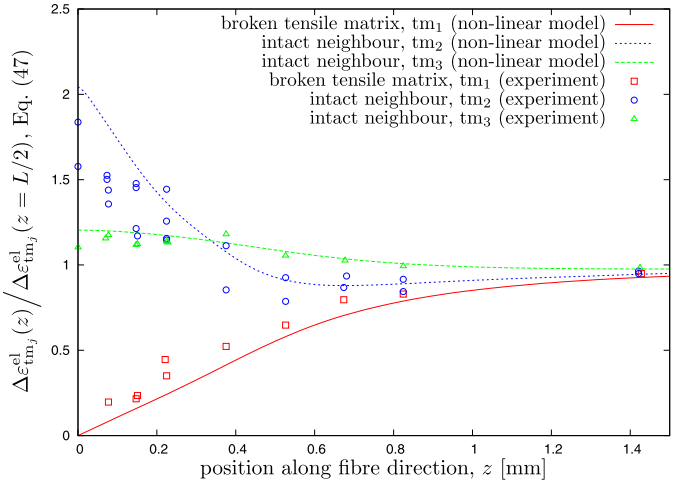

Fig. 9. Change in the tensile matrix elastic strains between the loaded and unloaded states. Predictions from the present model are compared with experimental data points taken from Figs. 10 and 11 of Hanan et al. (2003).

Hanan et al. (2003) also measured the change in the elastic strains,

$$\Delta\varepsilon^{el}_{f_i}(z) = \varepsilon^{el}_{f_i}(z)\Big|_{850\ \text{MPa}} - \varepsilon^{el}_{f_i}(z)\Big|_{0\ \text{MPa}}, \tag{46}$$

in the fibres after unloading from the peak load of 850 MPa. These measurements are compared with the predictions of the present model in Fig. 8. As before, broad agreement of the predictions and measurements is noted.

Finally, the change in the elastic matrix strains,

$$\Delta\varepsilon^{el}_{tm_j}(z) = \varepsilon^{el}_{tm_j}(z)\Big|_{850\ \text{MPa}} - \varepsilon^{el}_{tm_j}(z)\Big|_{0\ \text{MPa}}, \tag{47}$$

upon unloading from the peak load are considered in Fig. 9. The tensile matrix strains in the broken tm_1 and intact tm_3 are reasonably captured. However, the tensile matrix elastic strain in the intact matrix bay, tm_2, is over-estimated by the model near $z = 0$. Hanan et al. (2003) report larger error bars in their matrix strain measurements, than in their fibre strains. Yet, these are not big enough to explain the present discrepancy. They also report that the adjacent matrix bays, tm_2, were partially cut at $z \approx 0$ either during specimen preparation, or testing. Since a cut matrix bay will locally be more compliant than an intact one, it will take smaller loads, and therefore develop smaller elastic strains. This offers a

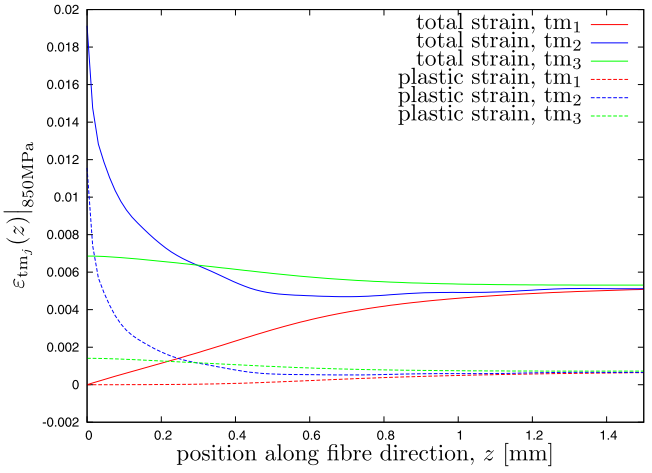

Fig. 10. Total and plastic strains in the tensile matrix elements tm_1, tm_2, and tm_3 predicted at the peak load of 850 MPa.

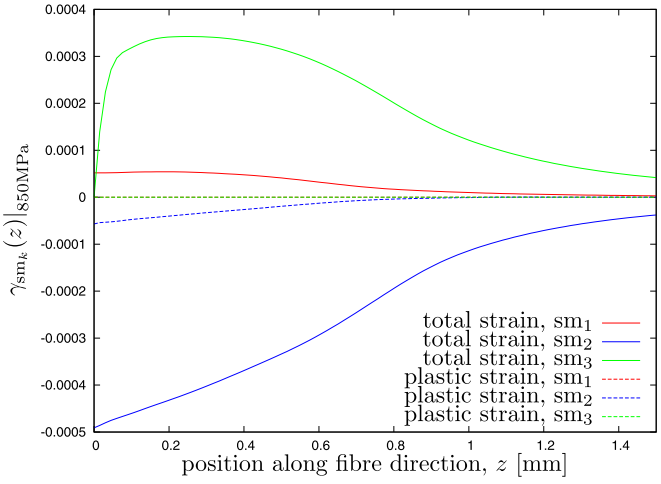

Fig. 11. Total and plastic shear strains in shearing matrix elements sm_1, sm_2, and sm_3 predicted at the peak load of 850 MPa.

plausible explanation for the smaller measured elastic strains in these bays.

8.2. Matrix plasticity and interfacial sliding

The mechanical fields in the vicinity of the breaks in the Hanan et al. (2003) composite predicted by the present non-linear model, corresponding to the peak imposed stress of $\sigma_c = 850$ MPa, are now presented.

Fig. 10 shows the total and plastic tensile strains in tensile matrix bays tm_1, tm_2, and tm_3 as a function of position. Both total and plastic strain in all the bays reach their far-field values at a distance of about 1.4 mm, or 10 fibre diameters. The far-field plastic strain is not zero, which implies that the matrix is undergoing gross yielding. The fraction of elastic strain to total strain decreases as the break plane, $z = 0$ mm is approached. In other words, the plastic strain becomes the more important as the break plane is approached.

The shear strains predicted in the shear matrix bays near the breaks is shown in Fig. 11. As noted previously in connection with Fig. 4, the sign of the shear strain simply indicates the state of breakage of the abutting tensile members, and is not in itself important. Plastic strains in the shear matrix are much more localised than that in the tensile matrix. Only the shear matrix bay sm_2, which is abutted by a broken fibre and an intact tensile matrix

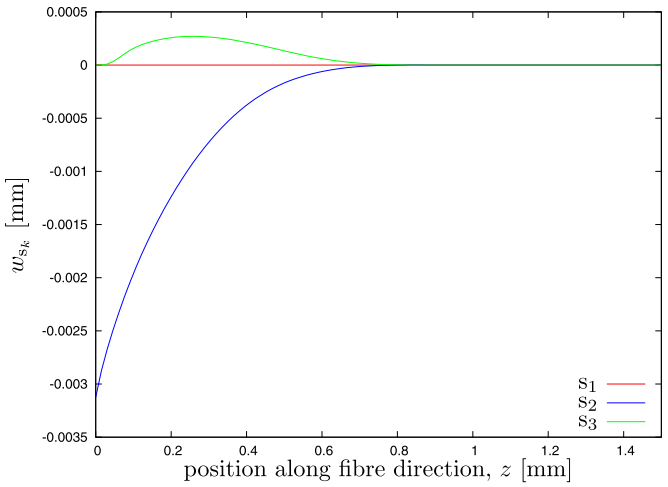

Fig. 12. Sliding displacements in sliding elements s_1, s_2, and s_3 predicted at the peak load of 850 MPa.

yields in shear. This is because shear stresses are developed only in the vicinity of breaks to transmit axial loads from intact to broken fibres.

The sliding displacements predicted in the sliding elements near the broken fibres are shown in Fig. 12. The sliding displacement is negligible in sliding elements whose abutting tensile elements are either both broken, e.g., s_1 or both intact, e.g., s_3. In element s_2, one of whose abutting tensile elements is broken, and the other intact, the sliding displacement is greatest, reaching as high as 3 μm at the break plane $z = 0$. This large displacement serves to blunt the shear stress in the associated shear matrix, sm_2, and blunts the stress concentration due to the breaks.

9. Discussion

A non-linear shear lag model of a metal matrix composite has been developed. This model accounts for fibre and matrix cracking, matrix plasticity, and fibre-matrix interfacial sliding. The model has been used to predict the elastic strains developed near a cluster of fibre and matrix breaks, both at a peak stress of 850 MPa and after unloading. The predictions compare well with the experimental measurements of Hanan et al. (2003). The role of the various elements of the present model in producing good agreement is discussed below in the context of the literature.

In a polymer matrix composite, Wagner et al. (1996) showed that the stress concentration in the intact neighbour of a broken fibre decreases with increasing fibre spacing. They used micro-Raman spectroscopy for their measurement. They attributed this observation to increasing tensile load the matrix, with decreasing fibre volume fraction. Since the Hedgepeth (1961) model entirely neglects the load carried by the matrix, it cannot account for the experimental observation. The MSSL model, due to Beyerlein and Landis (1999), is an effort to extend the Hedgepeth (1961) model to include matrix stiffness. The Beyerlein and Landis (1999) model, however, assumes linear elastic fibre and matrix elements. Zhang and Wang (2009) also considered the effect of matrix stiffness and also that of matrix yielding in tension. They however, unrealistically assumed that the yielding was localised to an infinitesimally thin strip in the matrix collinear with the adjacent fibre breaks. On the other hand, Landis and McMeeking (1999) proposed a shear-lag model assuming an elastoplastic matrix obeying J_2 flow theory. This model represents the most detailed accounting of the yielded state in the matrix. The matrix is assumed non-hardening. They found that for an elastically rigid matrix, the axial and shear stress

profiles approach the simple forms predicted by the simple sliding model, due to Kelly and Tyson (1965).

The loading of the present Ti matrix cannot be sufficiently described either by the linear model of Beyerlein and Landis (1999) or by the simple sliding model of Kelly and Tyson (1965). This is because the present matrix yields on the one hand grossly under the imposed load. On the other hand, the present $E_f/E_1 \approx 4$, so that the matrix cannot be assumed elastically rigid. Treating the matrix constitutive law using a flow theory, as in Landis and McMeeking (1999), in the multi-fibre composite is computationally expensive. Therefore, in the present work, matrix deformation is decomposed into tensile and shear parts, which are assumed uncoupled, following Zhou et al. (2002). The plastic and elastic strains in both the tensile matrix, and shear matrix elements, adjacent to the initially broken models elements, are comparable. Despite the decomposition of the matrix response into tensile and shear parts, it is seen that the present model captures the measured elastic strains well. This is consistent with a finding of Zhou et al. (2002) under dynamic loading conditions.

The importance of modelling the shear yielding of the matrix and interfacial debonding has been emphasised in the polymer matrix literature. Behzadi et al. (2009) compared the strains to failure predicted with and without accounting for matrix shear yielding with experimentally obtained values. They found that while both models overestimate the failure strain, the model with shear yielding produces the smaller overestimate. They attributed this to the reduced stress concentration in the fibres neighbouring broken ones when the matrix yields in shear. Accounting for both matrix strain yielding and interfacial debonding, Okabe and Takeda (2002) could capture the measured composite strength of a matrix. Mishnaevsky and Brøndsted (2009) studied the competition between interfacial debonding, and matrix cracking. The aforementioned mechanisms have been represented in the present model also. As in the aforementioned studies, these mechanisms are essential for the predictive success of the present model. Suppression of any of these mechanisms is found to lead to qualitatively poorer predictions in Section 8.1.

10. Conclusions

A non-linear shear lag model capable of accounting for multiple realistic damage modes in metal matrix composites and a fast computational algorithm for its solution have been developed. These failure modes are fibre breakage, matrix cracking, matrix plasticity, and fibre-matrix interfacial slippage. Model predictions have been compared with experimental results given in the literature and good agreement is found. The validated model has been used to elucidate the effects of non-linear material response near fibre breaks. Large differences in the mechanical fields have been found near the fibre breaks between the predictions of the present non-linear model, and that of a reduced linear model. This shows that fully accounting for these non-linearities is essential for obtaining good estimates of metal matrix composite reliability. This aspect will be discussed in future work.

References

Behzadi, S., Curtis, P., Jones, F., 2009. Improving the prediction of tensile failure in unidirectional fibre composites by introducing matrix shear yielding. Compos. Sci. Technol 69 (14), 2421–2427.

Beyerlein, I., Landis, C., 1999. Shear-lag model for failure simulations of unidirectional fiber composites including matrix stiffness. Mech. Mater 31 (5), 331–350.

Beyerlein, I., Phoenix, S., 1996. Stress concentrations around multiple fiber breaks in an elastic matrix with local yielding or debonding using quadratic influence superposition. J. Mech. Phys. Solids 44 (12), 1997–2039.

Budiansky, B., Hutchinson, J.W., Evans, A.G., 1986. Matrix fracture in fiber-reinforced ceramics. J. Mech. Phys. Solids 34 (2), 167–189.

Clyne, T., Withers, P., 1995. An Introduction to Metal Matrix Composites. Cambridge University Press.

Cox, H., 1952. The elasticity and strength of paper and other fibrous materials. Br. J. Appl. Phys 3 (3), 72.

Du, Z.-Z., McMeeking, R., 1994. Control of strength anisotropy of metal matrix fiber composites. J. Comput. Aided Mater. Des 1 (3), 243–264.

Fornberg, B., 1998. Classroom note: calculation of weights in finite difference formulas. SIAM Rev. 40 (3), 685–691.

Fornberg, B., 1998. A Practical Guide to Pseudospectral Methods. Cambridge Monographs on Applied and Computational Mathematics. Cambridge University Press.

González, C., Llorca, J., 2001. Micromechanical modelling of deformation and failure in Ti–6Al–4V/SiC composites. Acta Mater. 49 (17), 3505–3519.

Hanan, J., Üstündag, E., Beyerlein, I., Swift, G., Almer, J., Lienert, U., Haeffner, D., 2003. Microscale damage evolution and stress redistribution in Ti–SiC fiber composites. Acta Mater 51 (14), 4239–4250.

Hedgepeth, J.M., 1961. Stress concentrations in filamentary structures. Tech Rep. TN D 882, NASA.

Hedgepeth, J.M., Van Dyke, P., 1967. Local stress concentrations in imperfect filamentary composite materials. J. Compos. Mater 1 (3), 294–309.

Hill, R., 1998. The Mathematical Theory of Plasticity. Clarendon Press.

Jones, R., 2009. Deformation Theory of Plasticity. Bull Ridge Pub.

Kelly, A., Tyson, W., 1965. Tensile properties of fiber-reinforced metals. J. Mech. Phys. Solids 13, 329–350.

Landis, C.M., McMeeking, R.M., 1999. A shear-lag model for a broken fiber embedded in a composite with a ductile matrix. Compos. Sci. Technol. 59 (3), 447–457.

Mahesh, S., Hanan, J., Üstündag, E., Beyerlein, I., 2004. Shear-lag model for a single fiber metal matrix composite with an elasto-plastic matrix and a slipping interface. Int. J. Solids Struct. 41 (15), 4197–4218.

Martin, E., Carrére, N., 2012. Metal Matrix Composites: Continuous Silicon-Carbide Fibers/Titanium-Alloy Matrix. Wiley Encyclopedia of Composites.

Mishnaevsky, L., Brøndsted, P., 2009. Micromechanisms of damage in unidirectional fiber reinforced composites: 3D computational analysis. Compos. Sci. Technol. 69 (7), 1036–1044.

Moré, J.J., Garbow, B.S., Hillstrom, K.E., 1980. User Guide for Minpack-1. Tech. Rep. CM-P00068642.

Okabe, T., Takeda, N., 2002. Elastoplastic shear-lag analysis of single-fiber composites and strength prediction of unidirectional multi-fiber composites. Composites A 33 (10), 1327–1335.

Okabe, T., Takeda, N., Kamoshida, Y., Shimizu, M., Curtin, W., 2001. A 3D shear-lag model considering micro-damage and statistical strength prediction of unidirectional fiber-reinforced composites. Compos. Sci. Technol. 61 (12), 1773–1787.

Pimenta, S., Robinson, P., 2014. An analytical shear-lag model for composites with brick-and-mortar architecture considering non-linear matrix response and failure. Compos. Sci. Technol. 104, 111–124.

Preuss, M., Rauchs, G., Withers, P., Maire, E., Buffiere, J.-Y., 2002. Interfacial shear strength of Ti/SiC fibre composites measured by synchrotron strain measurement. Composites A 33 (10), 1381–1385.

Simo, J., Hughes, T., 2006. Computational Inelasticity. Interdisciplinary Applied Mathematics. Springer, New York.

Swolfs, Y., Gorbatikh, L., Verpoest, I., 2012. A 3D finite element analysis of static stress concentrations around a broken fibre. In: Proceedings of the 15th European Conference on Composite Materials, pp. 1–8.

Swolfs, Y., McMeeking, R.M., Verpoest, I., Gorbatikh, L., 2015. Matrix cracks around fibre breaks and their effect on stress redistribution and failure development in unidirectional composites. Compos. Sci. Technol. 108, 16–22.

Trefethen, L.N., 2013. Approximation theory and approximation practice. SIAM.

Wagner, H., Amer, M.S., Schadler, L.S., 1996. Fibre interactions in two-dimensional composites by micro-raman spectroscopy. J. Mater. Sci. 31 (5), 1165–1173.

Weideman, J.A., Reddy, S.C., 2000. A matlab differentiation matrix suite. ACM Trans. Math. Softw. 26 (4), 465–519.

Welsch, G., Boyer, R., Collings, E., 1993. Materials Properties Handbook: Titanium Alloys. ASM International.

Wessel, J.K., 2004. The Handbook of Advanced Materials: Enabling New Designs. John Wiley & Sons.

Winstone, M., Partridge, A., Brooks, J., 2001. The contribution of advanced high--temperature materials to future aero-engines. Proc. Inst. Mech. Eng. L J 215 (2), 63–73.

Xia, Z., Curtin, W., 2001. Multiscale modeling of damage and failure in aluminum–matrix composites. Compos. Sci. Technol 61 (15), 2247–2257.

Xia, Z., Curtin, W., Peters, P., 2001. Multiscale modeling of failure in metal matrix composites. Acta Mater. 49 (2), 273–287.

Zhang, J., Wang, F., 2009. Modeling of progressive failure in ductile matrix composites including local matrix yielding. Mech. Adv. Mater. Struct 16 (7), 522–535.

Zhou, Y., Huang, W., Xia, Y., 2002. A microscopic dynamic Monte Carlo simulation for unidirectional fiber reinforced metal matrix composites. Compos. Sci. Technol. 62 (15), 1935–1946.

Ziaja, W., 2009. Finite element modelling of the fracture behaviour of surface treated Ti-6Al-4V alloy. Arch. Comput. Mater. Sci. Surf. Eng 1, 53–60.